Influence of longitudinal spin fluctuations on the phase transition features in chiral magnets

A. M. Belemuk* and S. M. Stishov
Institute for High Pressure Physics, Russian Academy of Science, Troitsk 108840, Russia

(Received 9 February 2018; published 24 April 2018)

Using the classical Monte Carlo calculations, we investigate the effects of longitudinal spin fluctuations on the helimagnetic transition in a Heisenberg magnet with the Dzyaloshinskii-Moriya interaction. We use variable spin amplitudes in the framework of the spin-lattice Hamiltonian. It is this kind of fluctuations that naturally occur in an itinerant system. We show that the basic features of the helical phase transition are not changed much by the longitudinal spin fluctuations though the transition temperature T_c and the fluctuation hump seen in specific heat at $T > T_c$ is significantly affected. We report thermodynamic and structural effects of these fluctuations. By increasing the system size in the Monte Carlo modeling, we are able to reproduce the ring shape scattering intensity above the helimagnetic transition temperature T_c, which transforms into the spiral spots seen below T_c in the neutron scattering experiments.

DOI: 10.1103/PhysRevB.97.144419

I. INTRODUCTION

Several examples of helimagnets—metallic MnSi, FeGe, semiconductor $Fe_{1-x}Co_xSi$ [1], and insulating Cu_2OSeO_3 [2]—demonstrate remarkable features in their physical properties at the magnetic phase transition. These features originate from a first-order phase transition to the spiral state and the notable hump of fluctuation origin at temperatures slightly above T_c at zero magnetic field. They are clearly seen, e.g., in the heat capacity [3], thermal expansion [4], and ultrasound propagation and absorption [5] at the transition temperature T_c. In an applied magnetic field, these materials host chiral skyrmion lattices detected both by neutron scattering experiments [6] and the Lorentz transmission microscopy [7].

The mentioned magnetic materials crystallize in the noncentrosymmetric cubic space group $P2_13$, which results in the chiral Dzyaloshinskii-Moriya (DM) interaction. In the absence of the magnetic field, a competition between the ferromagnetic exchange J and the DM interaction D leads to a spiral magnetic order with the pitch axis aligned along the [111] crystallographic direction.

Apart from sharp anomalies connected with the helimagnetic transition, there are indications that strong spin fluctuations persist well above the helimagnetic transition temperature T_c. These are seen both in specific heat and magnetic susceptibility measurements and show up as well in neutron scattering experiments [8–12]. At high T, the neutron small angle scattering reveals ferromagnetic-like fluctuations that are well distributed over the whole $\mathbf{q}$ space. Close to T_c, strong chiral fluctuations that are localized in the spherical layer of a radius equal to the helix wave vector q_h are observed. Finally, at T_c, sharp magnetic Bragg spots appear in the $\langle 111 \rangle$ direction, signalizing the occurrence of a helical state [10,12].

Specific heat and susceptibility measurements in zero magnetic field [13–17] clarified the following nontrivial features of the phase transition in helimagnets. As the temperature decreases in the paramagnetic region, one observes a well-developed hump region in the specific heat, followed by a sharp spike at the onset of the helimagnetic order at T_c. Simultaneously, the magnetic susceptibility displays the Curie-Weiss law up to the hump region, then it reaches an inflection point followed by a maximum at T_c.

We report the results of Monte Carlo simulations of the classical spin system with variable spin amplitudes, which below we refer to as longitudinal spin fluctuations. So as opposed to other numerical works on this matter [18–22], we consider the spin length as a fluctuating variable. This is of special relevance to the itinerant electron system where magnetic and delocalized electron degrees of freedom are mutually interrelated [2,23]. Calculations with variable spin amplitudes complement results found in Ref. [24] for the spin-lattice model with unit spins.

The itinerant nature of magnetism in MnSi is most clearly seen in the difference of the magnetic moments per atom Mn in the magnetically ordered and paramagnetic phases. The magnetic moment per Mn atom in MnSi at low temperature was found to be $0.4\mu_B$, whereas the susceptibility data for the paramagnetic phase give an effective moment of $2.2\mu_B$ per Mn [25]. The importance of itinerant spin fluctuations was also demonstrated by the small-angle neutron scattering study of spin-wave dynamics of the full-polarized state of the Dzyaloshinskii-Moriya helimagnets [26]. It was found that the spin-wave stiffness for the MnSi helimagnet decreased twice as the temperature increased from zero to the critical temperature T_c.

Our understanding the itinerant-electron spin fluctuations was considerably advanced by Moriya [27] and Lonzarich and Taillefer [28], who explained quantitatively the magnetic properties of weak ferromagnets. While the account of longitudinal fluctuations is essential for understanding the properties of itinerant magnets like MnSi, the question how they affect magnetic phase transition is not fully clear [29]. In particular, the specific heat and magnetic susceptibility measured in the

*abel@hppi.troitsk.ru

itinerant magnet MnSi and the insulating magnetic material Cu_2OSeO_3 show quite a remarkable resemblance [2]. Moreover, both compounds host skyrmion phases and have similar magnetic phase diagrams [30].

Simulations of the thermodynamic properties of magnetic systems with an account of the temperature-induced longitudinal spin fluctuations have been elaborated previously in a number of works. The generalized Langevin spin dynamics algorithms treating both the longitudinal and transverse degrees of freedom of magnetic moments as dynamical variables on equal footing were developed in Refs. [31,32]. In Ref. [33], the authors studied the thermodynamics of itinerant magnets using a classical spin-fluctuation model with one parameter characterizing the degree of itineracy. They found that the magnetic short-range order, which is influenced by the presence of longitudinal spin fluctuations, is weak and almost independent on the degree of itineracy up to the strongly itinerant limit where the paramagnetic susceptibility is dominated by longitudinal fluctuations. The other procedure for calculating parameters of a high-temperature magnetic Hamiltonian, which utilizes transverse and longitudinal magnetic excitation spectra from first-principles calculations was developed in Ref. [34]. The calculated paramagnetic susceptibility and magnetic specific heat showed that the temperature-induced longitudinal spin fluctuations are essential for the correct explanation of high-temperature magnetism in Fe and Ni. Density functional calculations for multicomponent systems with weak and strong magnetic moments were further elaborated in Ref. [35].

In our model, we focus on the general features of the thermodynamics in helimagnets and use MnSi as an illustrative example. Our results show that longitudinal spin fluctuations do not change much the character of the helimagnetic phase transition but considerably affect the profile of the hump seen in the specific heat. We show that the essential contribution to the weight of the hump comes from the longitudinal fluctuations. It turns out that a distribution of chiral fluctuations that are built up in the hump region are consistent very well with the ring-shape structure of the Bragg intensity patterns seen in $\mathbf{q}$ space.

The outline of this paper is the following: the Hamiltonian for the spin lattice model and the details of MC simulation that includes variable spin amplitudes are given in Sec. II. In Sec. III, we show the results of calculations for the specific heat, magnetic susceptibility, and Bragg intensity patterns. Relevant comparisons with those measured in neutron scattering experiments are presented. Finally, Sec. IV, contains a conclusion.

II. MODEL AND SIMULATION BACKGROUND

A. Model

An accurate description of the full B20 structure of MnSi should include a calculation of magnetic interactions at the atomic level [36–40]. Nevertheless, for a description of slowly varying magnetic textures, one can treat the magnetic degrees of freedom as effective localized moments [41,42]. The volume of the system is partitioned into cells of linear size a, each cell is identified with classical Heisenberg spins $\mathbf{S}_i = (S_i^x, S_i^y, S_i^z)$. The lengths of spins in standard spin lattice models are fixed to unity. Instead, in our approach, we introduce variable spin amplitudes $S_i = |\mathbf{S}_i|$ fluctuating in a some range dS around $|\mathbf{S}_i| = 1$. The spins are arranged into a simple cubic lattice $L\times L\times L$, the lattice spacing is taken to be unity, $a = 1$.

The simplest Hamiltonian of this kind includes interaction between the nearest-neighbor and next-nearest neighbor spins, $H = H_J + H_D$ [18–21]. The first term,

$$H_J = -J\sum_{\mathbf{r}} \mathbf{S}_{\mathbf{r}}\cdot(\mathbf{S}_{\mathbf{r}+\hat{\mathbf{x}}}+\mathbf{S}_{\mathbf{r}+\hat{\mathbf{y}}}+\mathbf{S}_{\mathbf{r}+\hat{\mathbf{z}}}) - J'\sum_{\mathbf{r}} \mathbf{S}_{\mathbf{r}}\cdot(\mathbf{S}_{\mathbf{r}+2\hat{\mathbf{x}}}+\mathbf{S}_{\mathbf{r}+2\hat{\mathbf{y}}}+\mathbf{S}_{\mathbf{r}+2\hat{\mathbf{z}}}), \quad (1)$$

describes the ferromagnetic exchange interaction. The second term,

$$H_D = -D\sum_{\mathbf{r}}[\mathbf{S}_{\mathbf{r}}\times\mathbf{S}_{\mathbf{r}+\hat{\mathbf{x}}}\cdot\hat{\mathbf{x}}+\mathbf{S}_{\mathbf{r}}\times\mathbf{S}_{\mathbf{r}+\hat{\mathbf{y}}}\cdot\hat{\mathbf{y}}+\mathbf{S}_{\mathbf{r}}\times\mathbf{S}_{\mathbf{r}+\hat{\mathbf{z}}}\cdot\hat{\mathbf{z}}] - D'\sum_{\mathbf{r}}[\mathbf{S}_{\mathbf{r}}\times\mathbf{S}_{\mathbf{r}+2\hat{\mathbf{x}}}\cdot\hat{\mathbf{x}}+\mathbf{S}_{\mathbf{r}}\times\mathbf{S}_{\mathbf{r}+2\hat{\mathbf{y}}}\cdot\hat{\mathbf{y}}+\mathbf{S}_{\mathbf{r}}\times\mathbf{S}_{\mathbf{r}+2\hat{\mathbf{z}}}\cdot\hat{\mathbf{z}}], \quad (2)$$

describes the DM interaction with the DM vector directed along the corresponding bond direction. The summation is over the sites of the cubic lattice spanned by the vectors $\hat{\mathbf{x}}$, $\hat{\mathbf{y}}$, and $\hat{\mathbf{z}}$.

In this effective model, the true microscopic spin distribution is smeared within a cell of lattice size $\sim a$. The pitch length of the helices, λ_h, formed by the effective spins in a low-temperature phase is governed by the ratio D/J, $\tan 2\pi a/\lambda_h = D/J$. The values of effective parameters D and J can be essentially renormalized comparing with the microscopic ones, in particular the value of D can be the same order of magnitude as the exchange interaction J [18,19].

The Hamiltonian H, given by Eqs. (1) and (2), also includes interactions between the next-nearest neighbors, the corresponding amplitudes are J' and D'. It turns out that to map correctly the continuum model into a discrete one requires to include interactions with next-nearest neighbor spins. This compensates induced anisotropies originating from the discretization of the corresponding continuum spin model, as was first proposed by Buhrandt and Fritz [19]. Setting $J' = -J/16$ and $D' = -D/8$ allows to compensate these anisotropies in the Fourier transform of H up to fourth-order terms in momentum [19].

B. Monte Carlo simulation details

Classical Monte Carlo (MC) simulation with a standard single-site Metropolis algorithm is performed on a $L\times L\times L$ cubic lattice with periodic boundary conditions. In the calculations, we hold the parameter $J = 1$ fixed, serving as a unit of temperature. To implement the longitudinal spin fluctuation, we introduce spin amplitude variables S_i. The allowed range of fluctuations is limited by an amplitude dS, so that $(1 - dS) < S_i \leqslant 1$.

MC sweeps over the lattice are implemented differently for odd and even sweeps. For odd sweeps, only spin directions are allowed to be changed, as in the standard algorithm with unit spins. To update spin directions, we used two algorithms. In our main algorithm, a new spin direction is chosen within a cone with small angle $\Delta\theta$ near the direction of a given spin S_i [43]. During the equilibration, a value of $\Delta\theta$ is adjusted to keep, when possible, the acceptance rate around one-half. For some runs (for example, presented in Fig. 2 below) we

used uniform update algorithm, when a new spin direction is distributed uniformly over the unit sphere's surface [44]. At even MC sweeps, we update consecutively spin amplitudes at each lattice site as $S_i' = 1 - hdS$, where h is a random number from the interval $[0,1)$.

The simulation starts at some temperature well above T_c from some ordered, or random state. After the equilibration, we gradually decrease the temperature by sufficiently small steps $\Delta T = 10^{-2}$, near the transition temperature, the temperature steps were lowered to $\Delta T = 5\times10^{-3}$ (and in some runs to $\Delta T = 10^{-3}$). The equilibrated spin configuration is used as the initial spin configuration for the next run with lower temperature. At each temperature, we use 5×10^5 MC steps per spin (MCS) for equilibration and 10^6 MCS per spin to acquire the statistics. Most of results for the specific heat are obtained for lattice size $L = 30$. To check the dependence of data on the lattice size, some runs were carried out with $L = 60$ (correspondingly, with enlarged number of MCS). To minimize the finite size effects in the reciprocal space, we present Bragg intensity profiles calculated for the lattice size $L = 60$.

Energy and magnetization were recorded after each MC sweep to find MC thermal averages. The specific heat (per spin) was calculated by two ways, (i) from direct differentiation of the energy density $E(T) = \langle H\rangle/N$, where $N = L^3$, and (ii) in terms of energy fluctuations, $C = N\langle(\Delta E)^2\rangle/T^2$. These two methods give consistent results, the only discrepancy is seen at the transition temperature T_c, at which the energy $E(T)$ displays a finite jump. In the presented results we show the specific heat calculated from the differentiation of energy. Comparison of two ways of calculation is presented in Fig. 2 below. The magnetic susceptibility (per spin) is calculated in the usual way, $\chi(T) = N(\langle\mathbf{M}^2\rangle - \langle\mathbf{M}\rangle^2)/T$, where $\mathbf{M} = (1/N)\sum_i \mathbf{S}_i$.

Apart from the mean value of lattice spin, given by $\langle\mathbf{M}\rangle$, we also find at each T the thermal averaged lattice spin configuration $\langle\mathbf{S}_i\rangle$. This is used to find the thermal averaged Fourier components, $\langle\mathbf{S}_q\rangle = 1/N\sum_i\langle\mathbf{S}_i\rangle e^{-i\mathbf{q}\cdot\mathbf{R}_i}$, and subsequently, the Bragg intensity profile $I(\mathbf{q}) \propto |\langle\mathbf{S}_q\rangle|^2$. We present function $I(q_x,q_y,q_z)$ by corresponding sections in (q_x,q_y) and (q_x,q_z) planes of the $\mathbf{q}$ space.

To correctly present the spin spiral state

$$\mathbf{S}(\mathbf{R}_i) = S_Q\cos(\mathbf{Q}\cdot\mathbf{R}_i)\mathbf{e}_1 + S_Q\sin(\mathbf{Q}\cdot\mathbf{R}_i)\mathbf{e}_2 \qquad (3)$$

with unit vectors $\mathbf{e}_1$ and $\mathbf{e}_2$ being perpendicular to the spiral vector $\mathbf{Q}$, it is convenient to introduce a Bragg intensity profile projected onto the (q_x,q_y) plane, namely a function $I^*(q_x,q_y) = \sum_{q_z} I(q_x,q_y,q_z)$. Such a single spiral results in two Bragg peaks at $\mathbf{Q}$ and $-\mathbf{Q}$, seen as two separate spots in $I^*(q_x,q_y)$. We set $2\pi/L$ as a unit length in the reciprocal space, and the vectors $\mathbf{q}$ are scaled accordingly.

III. RESULTS AND DISCUSSION

To track the importance of longitudinal spin fluctuations, we examined three different series for variable spin amplitudes with $dS = 0,0.5$, and 1. In Fig. 1, we show the specific heat and magnetic susceptibility as functions of temperature for several values of DM interaction D and amplitudes dS. The specific heat features a smooth characteristic hump, which

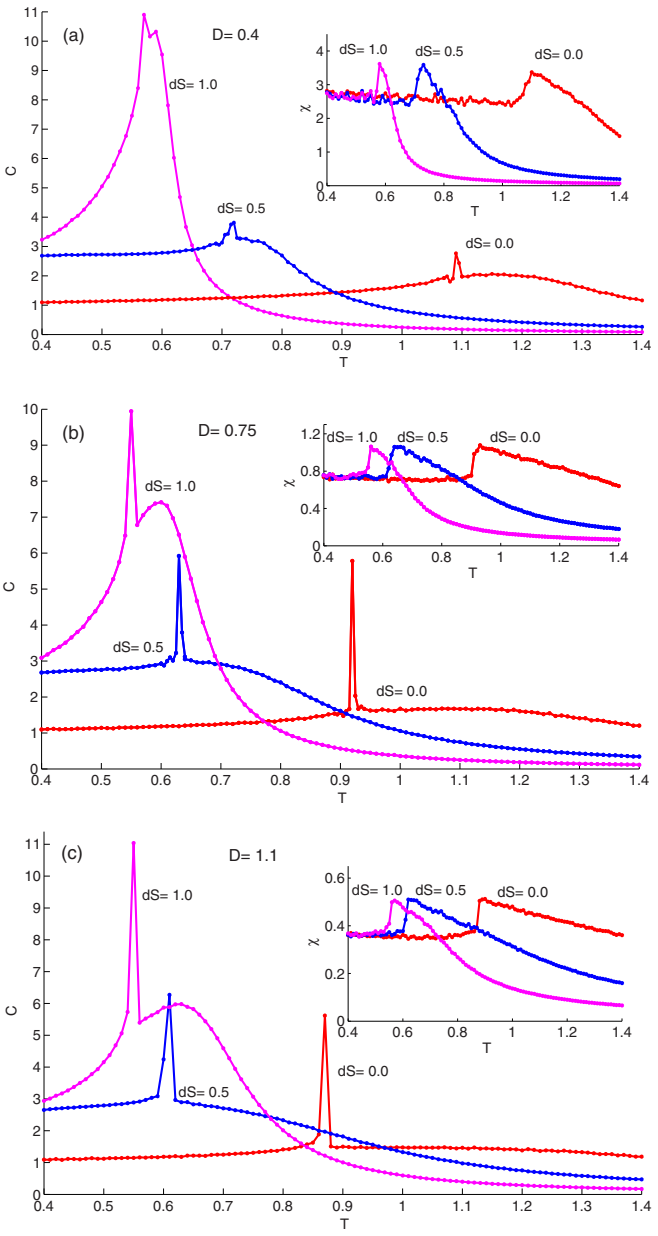

FIG. 1. Temperature dependence of the specific heat $C(T)$ for different values of the DM interaction $D = 0.4$ (a), 0.75 (b), and 1.1 (c) and spin amplitude fluctuation dS. (Inset) The corresponding dependencies of the magnetic susceptibility $\chi(T)$.

is substantially enhanced with increasing the dS amplitudes. The hump region is followed by an abrupt spike showing that the phase transition is first order, and signaling the onset of helimagnetic order seen in the Bragg intensity map in the form of two or four spots (see Figs. 3 and 4 below).

The spike in the specific heat at T_c shows a gradual development with increasing the parameter D. At small D [as $D = 0.4$ at panel (a)], the spike comes about in the form of fluctuations on the lower-temperature side of the hump. With increasing D, it gradually evolves into the sharp spikes at $D = 0.75$ [panel (b)] and $D = 1.1$ [panel (c)]. These spikes are seen both for rigid spins ($dS = 0$) and soft spins ($dS > 0$). Most notably, an inclusion of the spin amplitude fluctuations considerably

deforms the form of the $C(T)$ curve, namely, such fluctuations enhance the hump and shift it to lower temperatures.

A similar shift of the specific heat maximum due to longitudinal fluctuations was found in Ref. [32] from spin-dynamic simulations of the second-order phase transition in iron. The energy of the longitudinal spin fluctuations was used in the form of the Landau expansion $H_L = \sum_i (AS_i^2 + BS_i^4 + CS_i^6)$, which does not impose an upper limit on the magnitude of the on-site spin. In our simulation, on-site spins are less than unit, and in this regard the Landau expansion is approximated by hard-wall function, $H_L = E_0, S_i \leqslant 1$, $H_L = +\infty, S_i > 1$. An additional enhancement of the specific heat at low temperatures comes from the additional longitudinal degree of freedom included into the Hamiltonian. With increasing temperature, longitudinal fluctuations become saturated in our model and the behavior of $C(T)$ is entirely due to transverse spin fluctuations.

Comparing with the experimental results for the specific heat in MnSi and Cu_2OSeO_3 [2,5], one should note that the experimental $C(T)$ dependencies show a pronounced increase for $T < T_c$ and a well-developed hump for $T > T_c$. Our simulation results showing relatively flat dependencies of $C(T)$ for $dS = 0$ become closer to the experimental ones with an inclusion of spin amplitude fluctuations. This is particularly well seen for the dependencies $C(T)$ with $dS = 0.5$ and $dS = 1.0$ presented in Figs. 1(b) and 1(c).

Although the amplitude of longitudinal spin fluctuations can be as large as $dS = 1$, the resulting thermal average $\langle S \rangle = \langle |\mathbf{S}_i| \rangle$ very close, in fact, to $\langle S \rangle = 0.9$ at low temperatures ($T < T_c$) and $\langle S \rangle = 0.7 - 0.8$ in the hump region. This can be foreseen from energy considerations, too small values of $|\mathbf{S}_i|$ lead to considerable increase in the exchange and DM energy.

The magnetic susceptibility as a function of temperature for different values of dS is presented in the insets of Fig. 1. At $T > T_c$, the behavior of $\chi(T)$ shows a reasonable agreement with the experiment, namely for different values of D it bears a resemblance with the Curie-Weiss dependence, which is most clearly seen for larger values of dS. On approaching T_c, the susceptibility χ exhibits a well-defined peak, and finally, at $T < T_c$, a plateau is developed which is consistent with the measurements [15]. The amplitude of the peak strongly depends on parameter D and is nearly independent of the amplitude dS. However, the position of the peak depends on dS, and gradually shifts to lower temperatures with increasing dS, showing a resemblance with the corresponding behavior of T_c seen in the specific heat data.

In Fig. 2(a), we compare two specific heat curves, one obtained by differentiation of the energy and the other one by calculating thermal fluctuations of the energy. They show a remarkable coincidence almost at all temperatures. The only discrepancy appears around the transition temperature T_c and comes from a finite jump of energy $E(T)$ at T_c. A simulation with increased system size $L = 60$ is presented in Fig. 2(b). We see almost perfect agreement with the results for $L = 30$, the only mismatch is observed in the position of the specific heat peak and comes from the finite temperature steps used in the simulation.

To confirm unambiguously that the sharp spike seen in the specific heat comes from the first-order transition, we

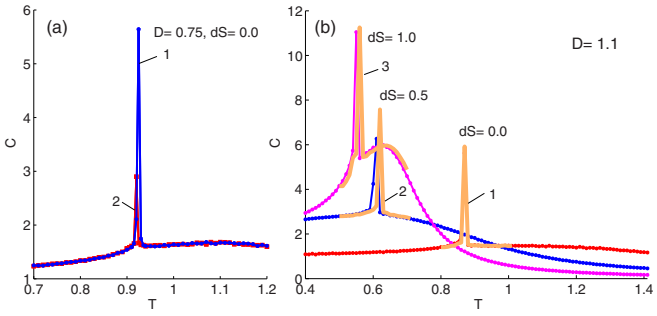

FIG. 2. (a) Specific heat obtained by differentiation of energy (curve 1) and from the fluctuation of energy (curve 2). (b) The specific heat for different system sizes, $L = 30$ (curves with markers) and $L = 60$ (presented by thick curves 1, 2, and 3 in limited temperature intervals).

examined the energy distribution function $P(E)$ at the corresponding transition temperatures. As is known, $P(E)$ demonstrates a two-peak structure at T_c if a transition is of first order. In Fig. 3, we show $P(E)$ calculated for various values of D and dS. First, in Fig. 3(a), we present $P(E)$ obtained by two different MC update algorithms used for the generation of a new spin configuration. The curves 1 corresponds to the algorithm when a new trial spin direction was generated within a cone of some fixed aperture angle, while curve 2 corresponds to the uniform algorithm at which the new trial direction was distributed uniformly. In these two cases, the transition from the paramagnet state to the helical ones passes through different intermediate states and the two curves excellently complement each other.

In Fig. 3(b), we compare energy distributions obtained for different dS. With increasing dS, the shape of $P(E)$ curve gradually tends to transform into a one-peak form. While the two-peak structure is still seen for a lower value $D = 0.75$ with $dS = 0$ [see inset Fig. 3(b)], two peaks are not resolved for larger dS although our data clearly demonstrate a small jump in the energy at T_c for $dS = 0.5$ and 1.0 (that jump leads to the spike in corresponding $C(T)$-dependance). The two-peak structure in $P(E)$ is not resolved also for small $D = 0.4$ [the corresponding $P(E)$ are not shown]. This is most probably due to the fact that the structure of function $P(E)$ becomes extremely sensitive in the proximity of T_c to resolve two-peaks at small D.

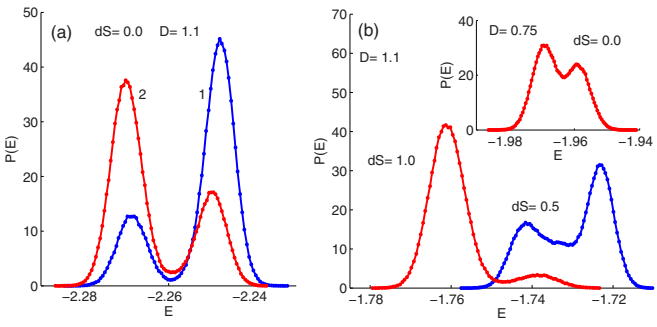

FIG. 3. [(a) and (b)] Energy distribution function $P(E)$ at T_c for different values of D and dS. Curves 1 and 2 in (a) correspond to the two different MC updates used for generation of new spin configurations.

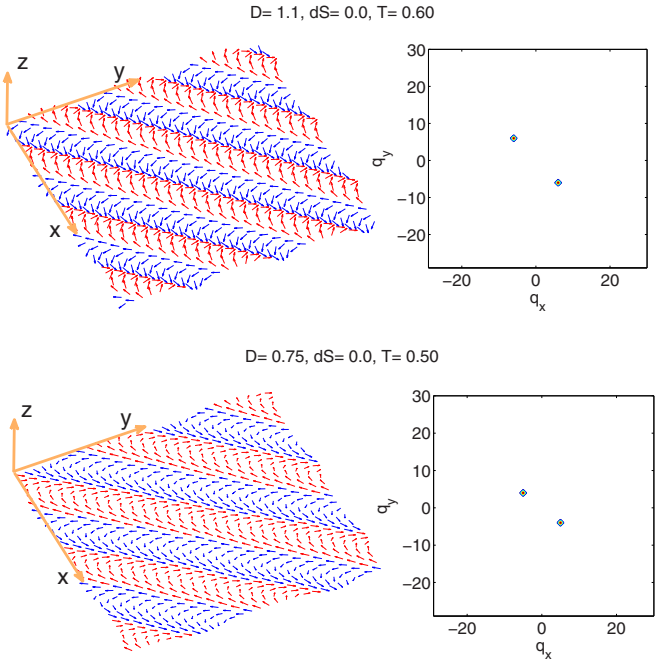

FIG. 4. Spin configuration $\langle \mathbf{S}_i \rangle$ in an xy plane (left) and a profile I^* of the Bragg intensity projected onto the (q_x, q_y) plane (right) for $dS = 0.0$, $D = 1.1$ (a), and $D = 0.75$ (b). Spins with positive S_z are marked as red and negative S_z as blue.

We now turn to the analysis of Bragg intensity (BI) patterns $I(\mathbf{q})$ in reciprocal space and their dependence on temperature, the corresponding results are given for system size $L = 60$. We also show the corresponding distributions of spins $\langle \mathbf{S}_i \rangle$ in xy plane $z = L/2$ (for clarity, only spins with coordinates $x_i, y_i \leqslant L/2$ are shown). To present BI spots in the reciprocal

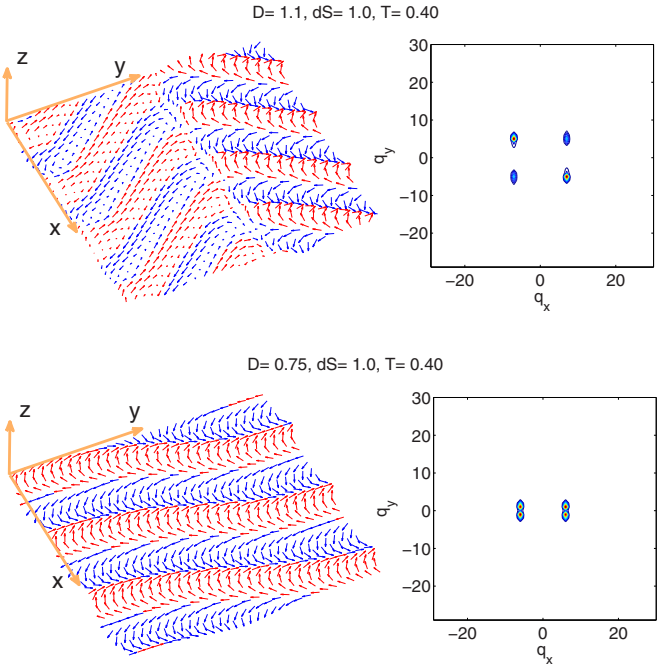

FIG. 5. Spin configuration $\langle \mathbf{S}_i \rangle$ and projected Bragg intensity profile I^* for $dS = 1.0$, $D = 1.1$ (a) and $D = 0.75$ (b). Designations are the same as in Fig. 4.

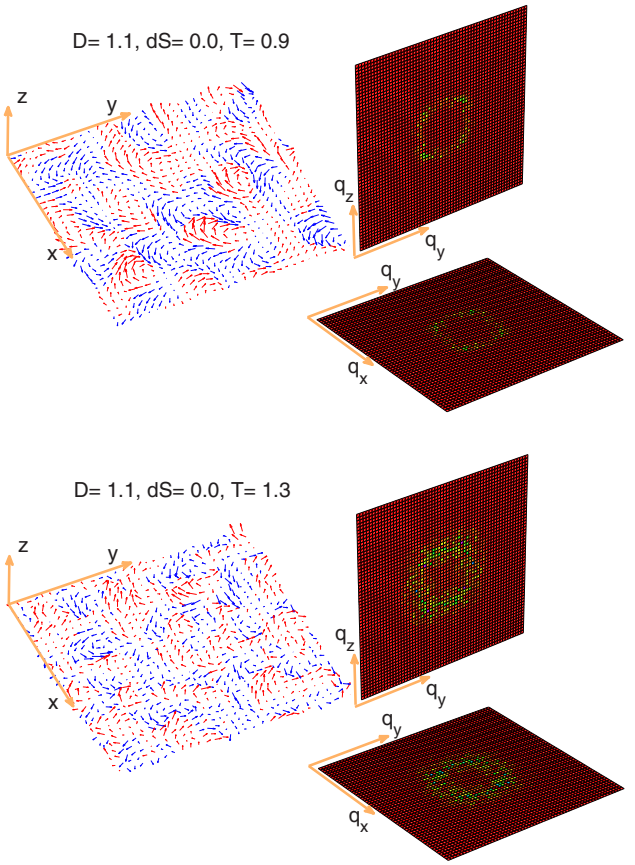

FIG. 6. Spin configuration $\langle \mathbf{S}_i \rangle$ in an xy plane (left) and cuts of Bragg intensity $I(\mathbf{q})$ by planes $q_x = 0$ (upper right) and $q_z = 0$ (lower right) for $D = 1.1, dS = 0.0$.

space coming from the spiral state we show the projected Bragg intensity $I^*(q_x, q_y)$, which has two spikes at points $\mathbf{q} = \pm\mathbf{Q}$ for a single spiral state and four spikes at points $\mathbf{q} = \pm\mathbf{Q}_1, \pm\mathbf{Q}_2$ for a two-spiral state.

Characteristic Bragg intensity profiles for the low-temperature phase are shown for the amplitudes $dS = 0$ and $dS = 1$ in Figs. 4 and 5, respectively. For the amplitude $dS = 0$, there are two spikes in $I^*(q_x, q_y)$, which correspond to a single spiral state of the helimagnet. The wave vector of the spiral is directed approximately along the cube diagonal, $\mathbf{Q} = 2\pi/L(-6,6,-5)$ for $D = 1.1$ and $\mathbf{Q} = 2\pi/L(-5,4,-3)$ for $D = 0.75$. For $dS = 1.0$, as seen from Fig. 5, the system exhibits a two-spiral state. There are four spikes in $I^*(q_x, q_y)$ at wave vectors $\mathbf{Q}_1 = 2\pi/L(-7,5,-5)$ and $\mathbf{Q}_2 = 2\pi/L(-7,-5,-5)$ for $D = 1.1$ and $\mathbf{Q}_1 = 2\pi/L(-6,1,-3)$ and $\mathbf{Q}_2 = 2\pi/L(-6,-1,-3)$ for $D = 0.75$. The spiral wave vectors $\mathbf{Q}_1$ and $\mathbf{Q}_2$ depend on parameter D and merge with each other with decreasing D. For low D, the corresponding spiral wave vector is directed along the direction [100]. The analysis of the corresponding spin configuration $\langle \mathbf{S}_i \rangle$ shows that two domains are formed in the system. At the boundary between domains, $|\langle \mathbf{S}_i \rangle|$ almost vanishes (most clearly it is seen for $D = 1.1$).

We further illustrate results for the Bragg intensity corresponding to the hump region in the $C(T)$ dependence. These are presented in Figs. 6 and 7 for the amplitudes $dS = 0$

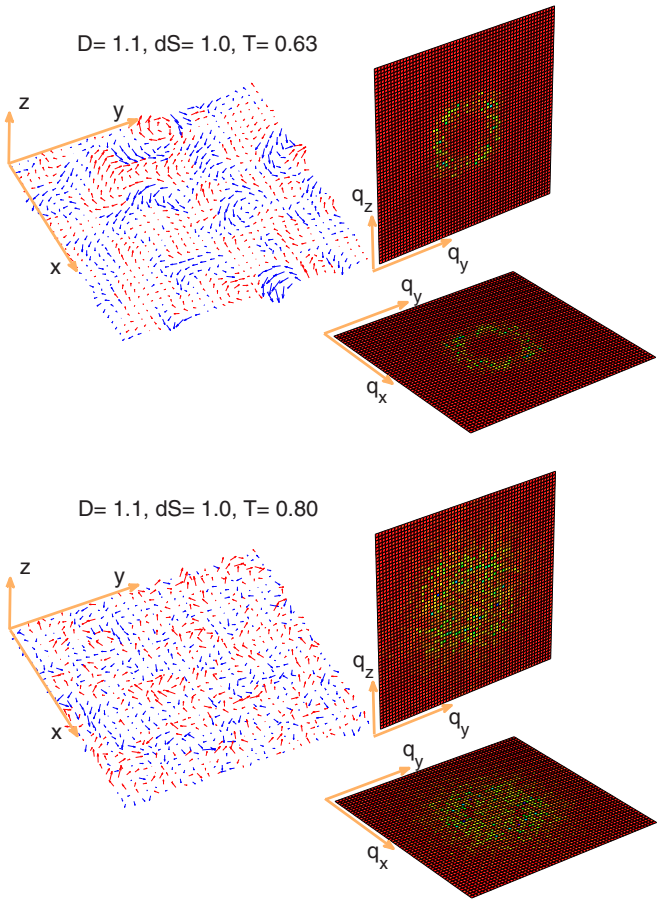

FIG. 7. The same as in Fig. 6 for $dS = 1.0$.

and $dS = 1$, respectively. We picked up two temperatures, the lower one approximately corresponds to the maximum of the hump, and the larger one is within the right slope of the hump. The left panel shows the averaged spin configuration $\langle \mathbf{S}_i \rangle$ at a given temperature in a single (x, y) plane. The two right panels show cuts of $I(\mathbf{q})$ in the $\mathbf{q}$ space taken in $q_x = 0$ (upper right panel) and $q_z = 0$ (bottom right panel) planes. The center of the planes is in the $\mathbf{q} = 0$ point and the cuts are limited by $-\pi/L \leqslant q_x, q_y, q_z \leqslant \pi/L$.

The key characteristic of the hump region is the ring-shape form of the BI function $I(\mathbf{q})$, which corresponds to the randomly oriented chiral spin fluctuations that persist above critical temperature T_c [8–10]. The ring is clearly seen at the maximum of the hump, at temperature $T = 0.9$ for $dS = 0$ and $T = 0.63$ for $dS = 1.0$. The radius of the ring q_h depends on the parameter D, it shrinks to zero with decreasing D.

On approaching T_c, the parameter q_h governs the pitch of the helix in the low temperature phase. The nature of the chiral fluctuations is most clearly seen from the inspection of the corresponding plots of the spin configurations. The ring-shape structure in the reciprocal space maps onto the vortexlike patterns of spins $\mathbf{S}_i$ in $\mathbf{r}$ space. On increasing the temperature, the ring becomes broader and eventually is smeared over the whole $\mathbf{q}$ space. The corresponding vortexlike patterns of spins are gradually melt out into a homogeneous random configuration. Such fluctuations are characteristic of the ferromagnetic systems with susceptibility $\chi(\mathbf{q}) \sim T/(q^2 + \kappa^2)$, where κ is the inverse correlation length [10]. We note that our calculations reproduce equally well the ring shape structure of spin fluctuations in reciprocal space both for rigid spins $dS = 0$ and with an inclusion of spin amplitude fluctuations $dS = 1.0$. However, the thickness of the ring depends on the amplitude of longitudinal fluctuations. For $dS = 0$, the weight of the hump is distributed over a larger temperature interval and the ring-shape structure of $I(\mathbf{q})$ persists over a wide temperature interval, while for $dS = 1.0$ it rapidly smears out with increasing temperature. The rapid smearing of the ring with increasing temperature in the MnSi experiments [8–10] suggests that the case with $dS = 1.0$ probably corresponds to the experimental situation.

IV. CONCLUSION

We presented a classical MC study of a helimagnet with competing exchange and DM interactions. Our simulation includes an additional degree of freedom, the variable spin amplitudes $|\mathbf{S}_i|$, that takes into account the itinerant nature of the magnetic moment in helimagnets like MnSi. The itinerant magnetic moments are especially pronounced in magnetic and thermodynamic measurements in MnSi [2,23]. Our study reveals that the behavior of the specific heat has two key features: the occurrence of a first-order transition at the helimagnetic transition temperature T_c seen as a spike in the $C(T)$ dependence, and the hump region above T_c with well-developed chiral fluctuations. The chiral fluctuation leads to a ring-shape structure of the Bragg intensity patterns in the reciprocal space. The results show that the amplitude of the chiral fluctuations in the hump region substantially depends on the amplitude of longitudinal fluctuations. In particular, the hump is greatly enhanced with increasing spin amplitude fluctuation dS. However, we have to conclude that the basic features of the helical phase transition are not changed drastically by the longitudinal spin fluctuations.

ACKNOWLEDGMENTS

We acknowledge discussions with V. N. Ryzhov. The work was supported by the Russian Foundation for Basic Research (Grants No. 17-52-53014 and No. 18-02-00183) (AMB and SMS) and the Russian Science foundation (Grant No. 17-12-01050) (SMS).

[1] M. Brando, D. Belitz, F. M. Grosche, and T. R. Kirkpatrick, Rev. Mod. Phys. **88**, 025006 (2016).

[2] V. A. Sidorov, A. E. Petrova, P. S. Berdonosov, V. A. Dolgikh, and S. M. Stishov, Phys. Rev. B **89**, 100403(R) (2014).

[3] S. M. Stishov, A. E. Petrova, S. Khasanov, G. K. Panova, A. A. Shikov, J. C. Lashley, D. Wu, and T. A. Lograsso, J. Phys.: Condens. Matter **20**, 235222 (2008).

[4] S. M. Stishov, A. E. Petrova, S. Khasanov, G. K. Panova, A. A. Shikov, J. C. Lashley, D. Wu, and T. A. Lograsso, Phys. Rev. B **76**, 052405 (2007).

[5] A. E. Petrova and S. M. Stishov, J. Phys.: Condens. Matter **21**, 196001 (2009).

[6] S. Mühlbauer, B. Binz, F. Jonietz, C. Pfleiderer, A. Rosch, A. Nebauer, R. Georgii, and P. Böni, Science **323**, 915 (2009).

[7] M. Nagao, Y.-G. So, H. Yoshida, K. Yamaura, T. Nagai, T. Hara, A. Yamazaki, and K. Kimoto, Phys. Rev. B **92**, 140415(R) (2015).

[8] S. V. Grigoriev, S. V. Maleyev, A. I. Okorokov, Y. O. Chetverikov, R. Georgii, P. Böni, D. Lamago, H. Eckerlebe, and K. Pranzas, Phys. Rev. B **72**, 134420 (2005).

[9] C. Pappas, E. Lelièvre-Berna, P. Falus, P. M. Bentley, E. Moskvin, S. Grigoriev, P. Fouquet, and B. Farago, Phys. Rev. Lett. **102**, 197202 (2009).

[10] S. V. Grigoriev, S. V. Maleyev, E. V. Moskvin, V. A. Dyadkin, P. Fouquet, and H. Eckerlebe, Phys. Rev. B **81**, 144413 (2010).

[11] L. J. Bannenberg, K. Kakurai, P. Falus, E. Lelièvre-Berna, R. Dalgliesh, C. D. Dewhurst, F. Qian, Y. Onose, Y. Endoh, Y. Tokura, and C. Pappas, Phys. Rev. B **95**, 144433 (2017).

[12] C. Pappas, L. J. Bannenberg, E. Lelièvre-Berna, F. Qian, C. D. Dewhurst, R. M. Dalgliesh, D. L. Schlagel, T. A. Lograsso, and P. Falus, Phys. Rev. Lett. **119**, 047203 (2017).

[13] S. M. Stishov, A. E. Petrova, A. A. Shikov, T. A. Lograsso, E. I. Isaev, B. Johansson, and L. L. Daemen, Phys. Rev. Lett. **105**, 236403 (2010).

[14] S. M. Stishov and A. E. Petrova, Phys. Rev. B **94**, 140406(R) (2016).

[15] A. Bauer, A. Neubauer, C. Franz, W. Münzer, M. Garst, and C. Pfleiderer, Phys. Rev. B **82**, 064404 (2010).

[16] A. Bauer and C. Pfleiderer, Phys. Rev. B **85**, 214418 (2012).

[17] M. Janoschek, M. Garst, A. Bauer, P. Krautscheid, R. Georgii, P. Böni, and C. Pfleiderer, Phys. Rev. B **87**, 134407 (2013).

[18] A. Hamann, D. Lamago, T. Wolf, H. v. Löhneysen, and D. Reznik, Phys. Rev. Lett. **107**, 037207 (2011).

[19] S. Buhrandt and L. Fritz, Phys. Rev. B **88**, 195137 (2013).

[20] S. D. Yi, S. Onoda, N. Nagaosa, and J. H. Han, Phys. Rev. B **80**, 054416 (2009).

[21] A. O. Leonov and M. Mostovoy, Nat. Commun. **6**, 8275 (2015).

[22] S. V. Isakov, J. M. Hopkinson, and H.-Y. Kee, Phys. Rev. B **78**, 014404 (2008).

[23] S. M. Stishov and A. E. Petrova, Phys. Usp. **54**, 1117 (2011)

[24] A. M. Belemuk and S. M. Stishov, Phys. Rev. B **95**, 224433 (2017).

[25] J. H. Wernick, G. K. Wertheim, and R. C. Sherwood, Mater. Res. Bull. **7**, 1431 (1972).

[26] S. V. Grigoriev, A. S. Sukhanov, E. V. Altynbaev, S.-A. Siegfried, A. Heinemann, P. Kizhe, and S. V. Maleyev, Phys. Rev. B **92**, 220415(R) (2015).

[27] T. Moriya, *Spin Fluctuations in Itinerant Electron Magnetism* (Springer-Verlag, Berlin, 1985).

[28] G. G. Lonzarich and L. Taillefer, J. Phys. C **18**, 4339 (1985).

[29] S. M. Stishov, Phys. Usp. **59**, 866 (2016).

[30] T. Adams, A. Chacon, M. Wagner, A. Bauer, G. Brandl, B. Pedersen, H. Berger, P. Lemmens, and C. Pfleiderer, Phys. Rev. Lett. **108**, 237204 (2012).

[31] O. Chubykalo-Fesenko, U. Nowak, R. W. Chantrell, and D. Garanin, Phys. Rev. B **74**, 094436 (2006).

[32] P.-W. Ma and S. L. Dudarev, Phys. Rev. B **86**, 054416 (2012).

[33] A. L. Wysocki, J. K. Glasbrenner, and K. D. Belashchenko, Phys. Rev. B **78**, 184419 (2008).

[34] A. V. Ruban, S. Khmelevskyi, P. Mohn, and B. Johansson, Phys. Rev. B **75**, 054402 (2007).

[35] M. Ležaić, P. Mavropoulos, G. Bihlmayer, and S. Blügel, Phys. Rev. B **88**, 134403 (2013).

[36] J. M. Hopkinson and H.-Y. Kee, Phys. Rev. B **74**, 224441 (2006).

[37] J. M. Hopkinson and H.-Y. Kee, Phys. Rev. B **75**, 064430 (2007).

[38] J. M. Hopkinson and H.-Y. Kee, Phys. Rev. B **79**, 014421 (2009).

[39] V. A. Chizhikov and V. E. Dmitrienko, Phys. Rev. B **85**, 014421 (2012).

[40] V. A. Chizhikov and V. E. Dmitrienko, Phys. Rev. B **88**, 214402 (2013).

[41] X. Z. Yu, Y. Onose, N. Kanazawa *et al.*, Nature (London) **465**, 901 (2010).

[42] P. Milde, D. Köhler, J. Seidel *et al.*, Science **340**, 1076 (2013).

[43] P. A. Serena, N. Garcia, and A. Levanyuk, Phys. Rev. B **47**, 5027 (1993).

[44] Z. Wang and C. Holm, J. Chem. Phys. **115**, 6351 (2001).